1   **Visualization of axonal protein allocation in *Drosophila* with whole-brain**

2   **localization microscopy**

3   **Authors:** Li-An Chu[1,2,#], Chieh-Han Lu[2,4,#,†], Shun-Min Yang[2], Kuan-Lin Feng[3], Yen-Ting

4   Liu[4], Chun-Chao Chen[1], Yun-Chi Tsai[4], Peilin Chen[4], Ting-Kuo Lee[2], Yeu-Kuang Hwu[2], Bi-

5   Chang Chen[4*], Ann-Shyn Chiang[1,2,3,5,6,7*]

6   **Affiliations:**

7   1. Brain Research Center, National Tsing Hua University, Hsinchu 30013, Taiwan

8   2. Institute of Physics, Academia Sinica, Taipei 11529, Taiwan

9   3. Institute of Systems Neuroscience, National Tsing Hua University, Hsinchu 30013,

10   Taiwan

11   4. Research Center for Applied Sciences, Academia Sinica, Taipei 11529, Taiwan

12   5. Department of Biomedical Science and Environmental Biology, Kaohsiung Medical

13   University, Kaohsiung 80780, Taiwan

14   6. Institute of Molecular and Genomic Medicine, National Health Research Institutes,

15   Zhunan, Miaoli 35053, Taiwan

16   7. Kavli Institute for Brain and Mind, University of California at San Diego, La Jolla, CA

17   92093-0526, USA

18   #These authors contributed equally to the project.

19   † Present address: Department of Genetics and Complex Diseases, Harvard T H Chan School

20   of Public Health, Boston, MA02115, United States

21   *Correspondence and requests for materials should be addressed to A.S.C. or B.C.C

22   Ann-Shyn Chiang, Brain Research Center, National Tsing Hua University,

23   101, Section 2, Kuang-Fu Road, Hsinchu 30013, Taiwan

24   Phone: 886-3-5742760; FAX: 886-3-5715934

1   Bi-Chang Chen, Research Center for Applied Sciences, Academia Sinica,

2   128 Sec. 2, Academia Rd., Nankang, Taipei 11529, Taiwan

3   Phone: 886-2-27873133; FAX: 886-2-27873122

4

1   **Abstract**

2   Long-term memory (LTM) formation requires learning-induced protein synthesis in

3   specific neurons and synapses within a neural circuit. Precisely how neural activity

4   allocates new proteins to specific synaptic ensembles, however, remains unknown. We

5   developed a deep-tissue super-resolution imaging tool suitable for single-molecule

6   localization in intact adult *Drosophila* brain, and focused on the axonal protein allocation

7   in mushroom body (MB), a central neuronal structure involved in olfactory memory

8   formation. We found that insufficient training suppresses LTM formation by inducing the

9   synthesis of vesicular monoamine transporter (VMAT) proteins within a dorsal paired

10   medial (DPM) neuron, which innervates all axonal lobes of the MB. Surprisingly, using

11   our localization microscopy, we found that these learning-induced proteins are distributed

12   only in a subset of DPM axons in specific sectors along the MB lobes. This neural

13   architecture suggests that sector-specific modulation of neural activity from MB neurons

14   gates consolidation of early transient memory into LTM.

15

1   **Introduction**

2   Memory formation requires learning-induced protein synthesis in specific neurons and

3   synapses within a neural circuit. In all species examined, there are two distinct phases of

4   memory formation: a transient neural activity associated with early memory and a protein-

5   synthesis-dependent change in synaptic connectivity associated with long-term memory

6   (LTM)[1,2]. Early memory is labile; sustained neural activity during this phase nonetheless is

7   crucial for the induction of LTM and its underlying protein synthesis, which occurs only in a

8   few neurons sparsely distributed throughout the brain[3-5]. Exactly how neural activity induces

9   protein synthesis in some but not all neurons in a circuit and then allocates new proteins to

10   specific synaptic ensembles during LTM formation, however, remains unknown.

11   Recent advances in super-resolution microscopy have allowed for localization of single

12   molecules within individual cells[6-8], but not within large tissues[9]. Our understanding of

13   memory formation may benefit from these advances by enabling us to visualize the allocation

14   of associative learning-induced proteins at the level of the synapse. In the present study, we

15   integrated several optical technologies to develop a deep-tissue imaging tool suitable for

16   single-molecule localization in an intact adult *Drosophila* brain. We show that insufficient

17   training suppresses LTM formation by inducing the synthesis of vesicular monoamine

18   transporter (VMAT) proteins in a single dorsal paired medial (DPM) neuron, which

19   innervates all axonal lobes of the mushroom body (MB). Consistent with this observation,

20   downregulation of VMAT or reduced serotonin synthesis in the DPM neuron enhances LTM

21   formation. Strikingly, we found that training-induced VMAT proteins are preferentially

22   allocated to a specific subset of DPM neurites, which arborize within the α2/β′1 MB sectors.

23   This neural architecture suggests that sector-specific serotonin modulation of neural activity

24   from MB neurons gates consolidation of early transient memory into LTM. Moreover, the

1   present study demonstrates that our single-molecule imaging technique can be used to

2   visualize memory allocation at specific synaptic ensembles within an intact brain.

3   **Results**

4   **Deep-tissue localization microscopy (DTLM)**

5   The study of memory formation requires novel tools for visualizing the allocation of

6   learning-induced proteins into synaptic ensembles in an intact brain. Several research groups

7   have attempted to modify super-resolution microscopy techniques for use with larger imaging

8   volumes[10-13]. Among these techniques, point accumulation for imaging in nanoscale

9   topography has achieved sub-100 nm resolution in samples over 20-μm thick by utilizing the

10   inherent optical sectioning of the lattice lightsheet to prevent premature photo-bleaching

11   (which limits localization and image quality)[13,14]. This method nonetheless fails to

12   compensate for tissue-induced aberrations, thereby restricting imaging depth and volume. To

13   visualize protein molecules within larger tissues, we integrated a Bessel beam lightsheet,

14   spontaneous blinking fluorophore, and optical tissue clearing to develop a deep-tissue

15   imaging tool suitable for single-molecule localization in an intact adult *Drosophila* brain (**Fig.**

16   **1a and Methods)**. The lightsheet was generated by scanning a Bessel beam created by

17   filtering the laser illumination with an annular ring mask at the Fourier plane, which was

18   conjugated to the back aperture of the excitation objective (customized, N.A. = 0.5, working

19   distance = 12.8 mm; NARLabs, ITRC, Taiwan; **Fig. 1b**)[15,16]. The Bessel beam has been

20   described as a self-reconstruction light beam that is particularly effective for penetrating into

21   a thick specimen[15,16]. The length of this lightsheet was extended from 50 μm to over 200 μm

22   using an axicon lens (**Supplementary Fig. 1a,b**). Through constructive interference at the

23   imaging plane, the energy distribution of the lightsheet is spatially confined within a 0.5-μm

24   layer, thereby reducing background signal and preventing unwanted photo-bleaching

1 (**Supplementary Fig. 1c,d**).

2 Traditional localization microscopy relies on two chemical mechanisms for the partial

3 activation of fluorophores: either an alternating two-wavelength exposure or a single-

4 wavelength high-intensity illumination[7,8,17]. Use of an additional activation laser, however,

5 prolongs image acquisition time and causes additional photo-bleaching due to short-

6 wavelength exposure. For high intensity illumination, the laser fluence deposited to the

7 sample rapidly consumes the photon budget and makes it unrealistic to achieve large scale

8 imaging. We addressed these problems by using a novel spontaneous blinking fluorophore,

9 HMSiR, which can be excited at a relatively low power density of 40 W/cm^2. Consequently

10 fluorophore blinking was extended to an area up to 75,000 μm^2 **(Fig. 1b)**. When combined

11 with the use of HMSiR and tissue clearing (ScaleView-A2)*[18]*, our DTLM method can

12 reconstruct super-resolution images of an entire adult brain **(Methods)**. Importantly, the

13 uncertainty of localized blinking events is similar through the entire z depth (**Fig. 1c**).

14 Typically, over 100 M particles are contained in each of the four sub-volumes used to

15 reconstruct DTLM images of the whole brain (**Supplementary Fig. 1e**), and the total

16 acquisition time is less than one day **(Methods)**. To analyze gigantic datasets of raw images

17 and reconstruct the whole fly brain at super-resolution, we created a parallel computing

18 pipeline based on ThunderSTORM[19] on a Lustre-backed Torque cluster (**Supplementary**

19 **Movie 1**, **Supplementary Fig. 2**).

20 The photoelectric sensors used for conventional fluorescence imaging (green fluorescent

21 protein, GFP) have a limited dynamic range. Thus, it can be difficult to capture structures

22 with weaker GFP signals in a single image (**Supplementary Fig. 5b, left**). Because DTLM

23 localizes individual molecules separately and reconstructs the image based on localization

24 events, it is insensitive to intensity differences, thereby enabling the capture of greater detail

25 in a single image. DTLM, for instance, captured a majority of parallel, densely bundled

1   neural fibers connecting the brain and body (**Supplementary Fig. 5b, middle**). When

2   sufficient localization density was achieved, individual brain-ascending/descending fibers

3   could be digitally segmented (**Supplementary Fig. 5b, right**). Furthermore, DTLM enabled

4   three-dimensional visualization of individual synaptic proteins (Down syndrome cell

5   adhesion molecules) within a single spine-like protrusion in a dendrite of the giant fiber

6   neuron (**Supplementary Fig. 5c**).

7   **Visualizing fine neurites in the whole brain**

8   Targeted genetic manipulations using the promoter-driven *TH-Gal4* line[20] have revealed that

9   dopaminergic neurons (DANs) are involved in various brain functions in *Drosophila*,

10   including decision making[21], arousal[22], and learning and memory[23]. To obtain a more

11   comprehensive understanding of these neural circuits underlying various behaviors, we used

12   single-molecule DTLM imaging to map the morphology and wiring patterns of all *TH-Gal4*

13   neurons in the adult brain (**Fig. 2**). Due to nominal photo-bleaching and optical clearing,

14   DTLM allowed us to image several overlapped sub-volumes under a high N.A. lens and

15   stitch them into a single big dataset of the entire brain at super-resolution. This large-volume

16   super-resolution map enabled simultaneous visualization of putative dopaminergic neurons

17   labelled with strong GFP signal in the central brain (**Supplementary Fig. 6**), as well as fine

18   neurites labelled with weak GFP signal in the optic lobe (**Fig. 2a)**. Serial optical slices and

19   three-dimensional navigation demonstrated extensive yet separable neurites (**Supplementary**

20   **Movie 3**). These high-quality images also allowed for digital segmentation of most individual

21   neurons, with nominal axial overlap (**Fig. 2b**). Next, we applied DTLM to visualize the

22   allocation of learning-induced new proteins.

23   **Suppression of LTM formation due to insufficient training**

1 *Drosophila* can learn to associate an odor with foot-shock punishment, and memory

2 formation thereafter exhibits several temporal phases, including protein synthesis-dependent

3 long-term memory[24,25]. The odor-shock association appears to occur in the MB, where the

4 conditioned odor stimulus is represented by the neural activity of a sparse subpopulation of

5 intrinsic Kenyon cells (KCs). The MB lobes can be subdivided into 15 consecutive sectors

6 based on their innervation by distinct types of DANs and MB output neurons (MBONs).

7 Evidence suggests that the unconditioned aversive stimulus is relayed via three types of

8 dopaminergic neurons innervating the α'1γ2, β2β'2, and γ1 sectors, respectively, thereby

9 modulating synaptic strength between KCs and MBONs and leading to conditioned

10 behaviours[4,5,26-29]. Multiple sessions of training with regular rest intervals (i.e., spaced

11 training) induce a transient increase in KC-MBON responses that eventually transforms into

12 stable LTM—a process that involves local protein synthesis in three types of MBONs

13 innervating the α3/β'1/β'2/γ3 sectors, respectively[4,5]. It remains unclear how this sector-

14 specific modulation occurs and leads to LTM storage in specific neurons and synapses

15 downstream of the MB.

16   The dorsal paired medial (DPM) neuron, on the other hand, is a single giant neuron with

17 extensive neurites that innervate all MB lobes, modulating KC-MBON activity by releasing

18 serotonin to sustain neural activity associated with an intermediate phase of anesthesia-

19 resistant memory (ARM)[27]. In aged flies, reduced DPM-MBON connectivity appears to

20 impair protein synthesis-dependent LTM[28]. Thus, ARM and LTM may be mutually

21 exclusive[28]. To address how DPM participates in memory formation, we first trained flies

22 with DPM serotonin levels reduced by adult-stage specific RNAi-mediated downregulation

23 of synthetic enzymes. Normally, flies form maximal 1-day memory after 10 sessions of

24 spaced training (10x spaced) but minimal memory after only three sessions of spaced training

25 (3x spaced). When serotonin signaling in the DPM neuron was reduced, 3x spaced training

1 now was sufficient to produce maximal 1-day memory (**Fig. 3a**). This enhanced LTM lasted

2 for at least 4 days and was not seen after 3x massed training (**Fig. 3a**), suggesting a bona-fide

3 protein-synthesis dependent LTM (and not ARM). With immunolabeling, we also observed a

4 significant increase in vesicular monoamine transporter (VMAT) proteins—which uptake

5 serotonin and other monoamines into presynaptic vesicles—at the DPM soma within 3 hours

6 after 3x spaced training (**Fig. 3b**). This increase in VMAT expression was abolished by acute

7 activation of temperature-sensitive RICIN[cs], a ribosomal toxin that inhibits protein

8 synthesis[3,30,31]. RNAi-mediated downregulation of VMAT yielded a decrease in anti-VMAT

9 intensity in the DPM soma (**Fig. 3c**) and also enhanced 1-day memory after 3x spaced

10 training (**Fig. 3d**). Together, these results suggest that insufficient spaced training suppresses

11 LTM formation by inducing VMAT synthesis and increasing serotonergic signaling from

12 DPM neurons.

13 **Visualizing synaptic VMAT molecules in DPM neurites**

14 To further examine how insufficient training-induced VMAT proteins regulate serotonin

15 release from DPM neurons in synapses, we used single-molecule DTLM imaging to quantify

16 changes in VMAT distribution among all DPM neurites before and after 3x spaced training

17 (**Fig. 4a**). By cropping the MB boundary, we determined the total number of immunolabeled

18 VMAT molecules in the MB. We classified these VMAT molecules into DPM+ and DPM-

19 groups based on the 3D digital intersection between VMAT and DPM (**Supplementary**

20 **Movie 4**). Importantly, this classification can be achieved only by using DTLM

21 (**Supplementary Fig. 7a**) and cannot be achieved with state-of-the-art confocal microscopy

22 (**Supplementary Fig. 7b**). The precision of DPM+ VMAT localization was demonstrated by

23 targeted $VMAT^{RNAi}$ expression, which reduced the total number of VMAT molecules in

24 DPM+ neurites but not in the DPM- regions of MB lobes (**Fig. 4b, Supplementary Fig. 7c).**

25 Next, we examined VMAT molecules throughout the DPM neurites before and 3 hours after

1 3x spaced training and found that their distributions are highly variable among different flies,

2 with a tendency to increase after training **(Supplementary Fig. 7d).** Unexpectedly, this

3 tendency was statistically insignificant (**Fig. 4b**), regardless of the increase in the soma (**Fig.**

4 **3b**). Connectomic electron microscopy (EM) tracing of the $\alpha1/\alpha2/\alpha3$ MB sectors indicates

5 that the DPM neuron synapses with DANs/KCs/MBONs to form intricate sector-specific

6 networks[32,33]. These DPM neurites exhibit branch-specific neural activity (memory traces)

7 after associative learning[34], prompting us to investigate whether 3x spaced training induced

8 VMAT expression in some but not all sectors of DPM neurites.

9 **MB sector-specific increases in DPM VMAT molecules induced by space training**

10 We manually segmented DPM neurites into 15 MB sectors based on methods utilized in a

11 previous study[35] (**Supplementary Fig. 8 and Methods**). Quantitative analysis revealed that

12 the density of VMAT molecules in DPM+ neurites increased after training in the $\alpha2$ and $\beta'1$

13 sectors but not in the remaining MB sectors or in DPM- regions, when compared to that in

14 naïve flies **(Fig. 4c, d**). These increases appeared to be evenly distributed in the affected

15 sectors. In naive flies that had not undergone training, the distribution of VMAT molecules

16 was highly variable between DPM+ and DPM- neurites and among different sectors (**Fig. 4c**).

17 **Discussion**

18 Spatiotemporal allocation of associative learning-induced VMAT molecules suggests that

19 DPM neurons regulate memory formation via serotonergic modulation of DAN/KC/MBON

20 circuits in specific MB sectors. Translational regulation may account for this sector-specific

21 allocation, as increases in VMAT are (i) regulated by Fragile X mental retardation protein,

22 which itself is involved in olfactory LTM formation[36,37] and (ii) blocked by inhibition of

23 protein synthesis (**Fig. 3d**). Transcriptional regulation may also be implicated, as increases in

24 VMAT expression after training occur in both the soma and neurites of DPM neurons (**Figs.**

1   **3 and 4**). Previous studies have suggested that training induces local protein synthesis in

2   α3/β′1/β′2/γ3 MBONs during LTM consolidation[4,5]. The findings of the present study

3   suggest that modulation of serotonergic signaling (via VMAT) from DPM neurons to sector-

4   specific MB neurons also contributes to LTM consolidation during the first few hours after

5   training (**Fig. 3d**) but not during LTM retrieval[38]. Further studies are required to determine

6   whether α2/β′1-VMATs in the DPM directly and specifically modulate the function of

7   α2/β′1 MBONs. Although α2 MBONs exhibit highly variable functional responses among

8   individual subjects[39], their outputs appear necessary during LTM retrieval[39]. In contrast, β′1

9   MBONs appear to be involved in the forgetting process[40].

10   Neural plasticity involves local protein synthesis in both presynaptic axon terminals and

11   postsynaptic dendrite spines[41]. In *Drosophila* olfactory memory formation, postsynaptic

12   regulation of protein synthesis has been demonstrated[4,5], and here we present data suggesting

13   presynaptic regulation of protein synthesis during memory formation, as well. Using deep-

14   tissue localization microscopy, we further extend the visualization of protein allocations in a

15   few target neurons to a systems level of analysis. Consistent with branch-specific functional

16   responses during associative learning[34], our finding of sector-specific allocation of

17   presynaptic VMAT proteins in DPM neurons adds another layer of coding complexity to the

18   DANs/KCs/MBONs circuit within the MB. Spatiotemporal VMAT-mediated serotonin

19   release from DPM axons then directly modulates the neural activity of a subset of KCs within

20   specific MB sectors. Such serotonergic signaling helps to translate transient neural activity in

21   the MB circuit during early memory into LTM that includes postsynaptic regulation of

22   protein synthesis in specific MBONs.

23   One limitation of our current imaging method is that the precision of axial localization is

24   restricted by the thickness of the Bessel lightsheet (~500 nm), which is much less than the

25   precision at the lateral plane (~30 nm). Thus, separating entangled neurites is trivial at X-Y

1   plane but not always reliable along the Z axis. In this study, we corrected for this Z-plane

2   limitation by classifying VMAT immune-positive signals into DPM+ versus DPM- groups.

3   This approach was reasonably reliable because all imaged neurites in the MB derived from a

4   single DPM neuron. In future studies, the Z-axis resolution may be improved further (i) by

5   optical clearing using a medium with a higher refractive index[42] matched with a higher-

6   aperture objective, (ii) by using a cylindrical lens to refine the Z position[43], and/or (iii) by

7   combining DTLM with expansion microscopy[44]. With imaging near isotropic super-

8   resolution, visualization of the connectome representing LTM-dependent neuroplasticity

9   among all synaptic connections in an intact fly brain soon will be achievable[3-5].

10

11   **References**

12   1   Kandel, E. R., Dudai, Y. & Mayford, M. R. The molecular and systems biology of

13   memory. *Cell* **157**, 163-186 (2014).

14   2   Tonegawa, S., Pignatelli, M., Roy, D. S. & Ryan, T. J. Memory engram storage and

15   retrieval. *Curr Opin Neurobiol* **35**, 101-109 (2015).

16   3   Chen, C. C. *et al.* Visualizing long-term memory formation in two neurons of the

17   *Drosophila* brain. *Science* **335**, 678-685 (2012).

18   4   Pai, T. P. *et al. Drosophila* ORB protein in two mushroom body output neurons is

19   necessary for long-term memory formation. *Proc Natl Acad Sci U S A* **110**, 7898-7903

20   (2013).

21   5   Wu, J. K. *et al.* Long-term memory requires sequential protein synthesis in three subsets

22   of mushroom body output neurons in *Drosophila*. *Sci Rep* **7**, 7112, doi:10.1038/s41598-

23   017-07600-2 (2017).

6   Hell, S. W. & Wichmann, J. Breaking the diffraction resolution limit by stimulated emission: stimulated-emission-depletion fluorescence microscopy. *Opt Lett* **19**, 780-782 (1994).

7   Rust, M. J., Bates, M. & Zhuang, X. Sub-diffraction-limit imaging by stochastic optical reconstruction microscopy (STORM). *Nat Methods* **3**, 793-795 (2006).

8   Betzig, E. *et al.* Imaging intracellular fluorescent proteins at nanometer resolution. *Science* **313**, 1642-1645 (2006).

9   Spuhler, I. A., Conley, G. M., Scheffold, F. & Sprecher, S. G. Super resolution imaging of genetically labeled synapses in *Drosophila* brain tissue. *Front Cell Neurosci* **142**, 1-10 (2016).

10 Vaziri, A., Tang, J., Shroff, H. & Shank, C. V. Multilayer three-dimensional super resolution imaging of thick biological samples. *Proc Natl Acad Sci U S A* **105**, 20221-20226 (2008).

11 Abrahamsson, S. *et al.* Fast multicolor 3D imaging using aberration-corrected multifocus microscopy. *Nat Methods* **10**, 60-63 (2013).

12 Cella Zanacchi, F. *et al.* Live-cell 3D super-resolution imaging in thick biological samples. *Nat Methods* **8**, 1047-1049 (2011).

13 Legant, W. R. *et al.* High-density three-dimensional localization microscopy across large volumes. *Nat Methods* **13**, 359-365 (2016).

14 Schueder, F. *et al.* Multiplexed 3D super-resolution imaging of whole cells using spinning disk confocal microscopy and DNA-PAINT. *Nat Commun* **8**, 2090 (2017).

15 Fahrbach, F. O. & Rohrbach, A. Propagation stability of self-reconstructing Bessel beams enables contrast-enhanced imaging in thick media. *Nat Commun* **3**, 632 (2012).

16 Gao, L., Shao, L., Chen, B. C. & Betzig, E. 3D live fluorescence imaging of cellular dynamics using Bessel beam plane illumination microscopy. *Nat Protoc* **9**, 1083-1101 (2014).

17 Heilemann, M. *et al.* Subdiffraction-resolution fluorescence imaging with conventional fluorescent probes. *Angew Chem Int Ed Engl* **47**, 6172-6176 (2008).

18 Hama, H. *et al.* Scale: a chemical approach for fluorescence imaging and reconstruction of transparent mouse brain. *Nat Neurosci* **14**, 1481-1488, (2011)

19 Ovesny, M., Krizek, P., Borkovec, J., Svindrych, Z. & Hagen, G. M. ThunderSTORM: a comprehensive ImageJ plug-in for PALM and STORM data analysis and super-resolution imaging. *Bioinformatics* **30**, 2389-2390 (2014).

20 Friggi-Grelin, F. *et al.* Targeted gene expression in *Drosophila* dopaminergic cells using regulatory sequences from tyrosine hydroxylase. *J Neurobiol* **54**, 618-627 (2003).

21 Zhang, K., Guo, J. Z., Peng, Y., Xi, W. & Guo, A. Dopamine-mushroom body circuit regulates saliency-based decision-making in *Drosophila*. *Science* **316**, 1901-1904 (2007).

22 Andretic, R., van Swinderen, B. & Greenspan, R. J. Dopaminergic modulation of arousal in *Drosophila*. *Curr Biol* **15**, 1165-1175 (2005).

23 Waddell, S. Reinforcement signalling in *Drosophila*; dopamine does it all after all. *Curr Opin Neurobiol* **23**, 324-329 (2013).

24 Dubnau, J. & Chiang, A. S. Systems memory consolidation in *Drosophila*. *Curr Opin Neurobiol* **23**, 84-91 (2013).

25 Cognigni, P., Felsenberg, J. & Waddell, S. Do the right thing: neural network mechanisms of memory formation, expression and update in *Drosophila*. *Curr Opin Neurobiol* **49**, 51-58 (2018).

26 Aso, Y. *et al.* Three dopamine pathways induce aversive odor memories with different stability. *PLoS Genet* **8**, e1002768 (2012).

27   Lee, P. T. *et al.* Serotonin-mushroom body circuit modulating the formation of anesthesia-resistant memory in *Drosophila*. *Proc Natl Acad Sci U S A* **108**, 13794-13799 (2011).

28   Isabel, G., Pascual, A. & Preat, T. Exclusive consolidated memory phases in *Drosophila*. *Science* **304**, 1024-1027 (2004).

29   Tonoki, A. & Davis, R. L. Aging impairs protein-synthesis-dependent long-term memory in *Drosophila*. *J Neurosci* **35**, 1173-1180 (2015).

30   Endo, Y., Mitsui, K., Motizuki, M. & Tsurugi, K. The mechanism of action of ricin and related toxic lectins on eukaryotic ribosomes. The site and the characteristics of the modification in 28 S ribosomal RNA caused by the toxins. *J Biol Chem* **262**, 5908-5912 (1987).

31   Endo, Y. & Tsurugi, K. RNA N-glycosidase activity of ricin A-chain. Mechanism of action of the toxic lectin ricin on eukaryotic ribosomes. *J Biol Chem* **262**, 8128-8130 (1987).

32   Aso, Y. & Rubin, G. M. Dopaminergic neurons write and update memories with cell-type-specific rules. *Elife* **5** (2016).

33   Takemura, S. Y. *et al.* A connectome of a learning and memory center in the adult *Drosophila* brain. *Elife* **6** (2017).

34   Yu, D., Keene, A. C., Srivatsan, A., Waddell, S. & Davis, R. L. *Drosophila* DPM neurons form a delayed and branch-specific memory trace after olfactory classical conditioning. *Cell* **123**, 945-957 (2005).

35   Aso, Y. et al. The neuronal architecture of the mushroom body provides a logic for associative learning. *Elife* **3** (2014).

36 Tauber, J. M., Vanlandingham, P. A. & Zhang, B. Elevated levels of the vesicular monoamine transporter and a novel repetitive behavior in the *Drosophila* model of fragile X syndrome. *PLoS One* **6**, e27100 (2011).

37 Bolduc, F. V., Bell, K., Cox, H., Broadie, K. S. & Tully, T. Excess protein synthesis in *Drosophila* fragile X mutants impairs long-term memory. *Nat Neurosci* **11**, 1143-1145 (2008).

38 Keene, A. C., Krashes, M. J., Leung, B., Bernard, J. A. & Waddell, S. *Drosophila* dorsal paired medial neurons provide a general mechanism for memory consolidation. *Curr Biol* **16**, 1524-1530 (2006).

39 Hige, T., Aso, Y., Rubin, G. M. & Turner, G. C. Plasticity-driven individualization of olfactory coding in mushroom body output neurons. *Nature* **526**, 258-262 (2015).

40 Shuai, Y. *et al.* Dissecting neural pathways for forgetting in *Drosophila* olfactory aversive memory. *Proc Natl Acad Sci U S A* **112**, E6663-6672 (2015).

41 Younts, T. J. *et al.* Presynaptic protein synthesis is required for long-term plasticity of GABA release. *Neuron* **92**, 479-492 (2016).

42 Long, X., Colonell, J., Wong, A. M., Singer, R. H. & Lionnet, T. Quantitative mRNA imaging throughout the entire *Drosophila* brain. *Nat Methods* **14**, 703-706 (2017).

43 Huang, B., Wang, W., Bates, M. & Zhuang, X. Three-dimensional super-resolution imaging by stochastic optical reconstruction microscopy. *Science* **319**, 810-813 (2008).

44 Chen, F., Tillberg, P. W. & Boyden, E. S. Optical imaging. Expansion microscopy. *Science* **347**, 543-548 (2015).

Acknowledgments

Author contributions: L.A.C. and C.H.L. planned and performed the imaging experiments and image processing. L.A.C. performed immunostaining experiments. C.H.L, Y.T.L, and B.C.C. designed and constructed the DTLM. S.M.Y. produced the HMSiR conjugates. K.L.F. and C.C.C. planned and performed the behavioral experiments. Y.T.L. designed the automated blinking image processing protocol and software. L.A.C. performed image analysis. L.A.C., C.H.L., B.C.C. and A.S.C. wrote the manuscript. B.C.C and A.S.C. planned and managed the project.

Competing interests: The authors declare no competing financial interests. Readers are welcome to comment on the online version of the paper.

Data and materials availability: Requests for materials should be addressed to B.C.C. (chenb10@gate.sinica.edu.tw) or A.S.C. (aschinag@life.nthu.edu.tw).

1 **Figures and figure legends**
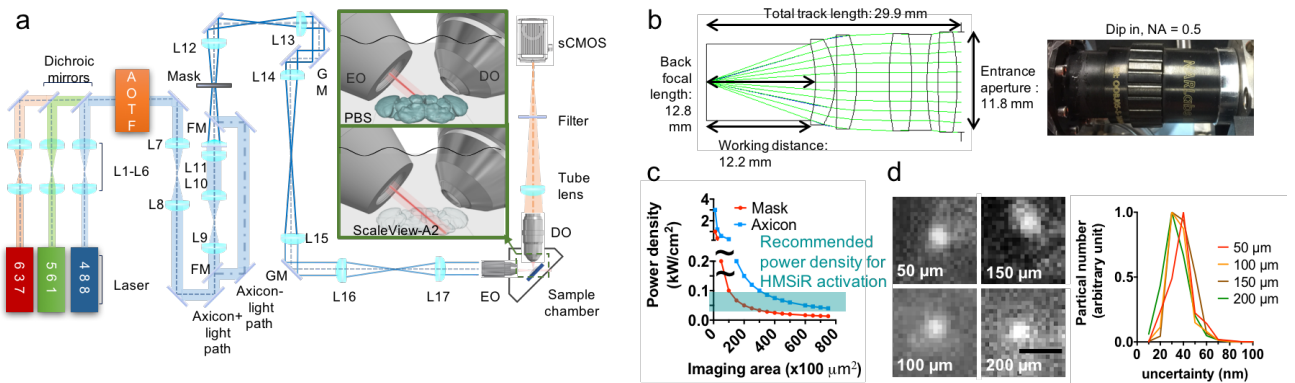
2

3 **Fig. 1. Bessel beam lightsheet for deep-tissue localization microscopy (DTLM). (a)** The

4 schematic configuration of the DTLM system. Inset: the geometry of relative positions

5 between two objective lenses and the specimen. AOTF: acoustic-optical tuneable filter; EO,

6 excitation objective; DO, detection objective; GM: galvo mirror; L: lens. **(b)** A customized

7 dip-in objective lens matching refractive index of ScaleView-A2 at a long working distance

8 of 12.2 mm. Left, Photograph of the lens. Right, Schematic design and simulated ray tracing.

9 **(c)** The lightsheet generated using an axicon lens carries higher power density than that

10 generated using the mask only. At the power density (40 w/cm^2) for HMSiR excitation, the
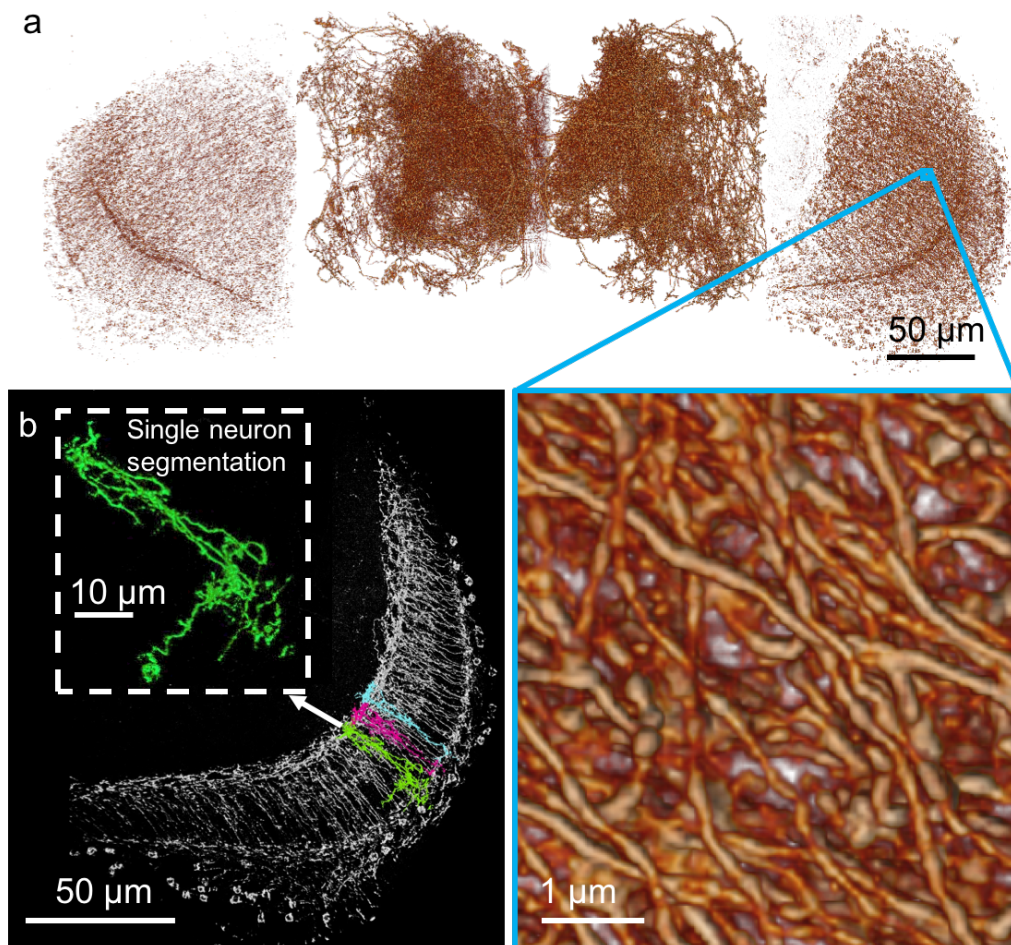
11 maximum lightsheet areas are 25,000 μm^2 and 75,000 μm^2, generated using a mask only and

12 an axicon lens, respectively. **(d)** Representative HMSiR blinking events (left) and overall

13 lateral uncertainty distribution (right) at four different depths in the fly brain cleared with

14 ScaleView-A2. Scale bar = 1 μm.

15

**Fig. 2. Single-molecule deep-tissue localization microscopy (DTLM) imaging of dopaminergic neurons (DANs) in the whole *Drosophila* brain.** **(a)** Volume rendering of whole-brain DANs. Zoom-in images show distinguishable interweaved neurites. **(b)** Digital segmentation of local neurons in the medulla. Inset: enlarged green neuron. The experimental flies carried *TH-Gal4*; *UAS-GCaMP6f* transgenes.
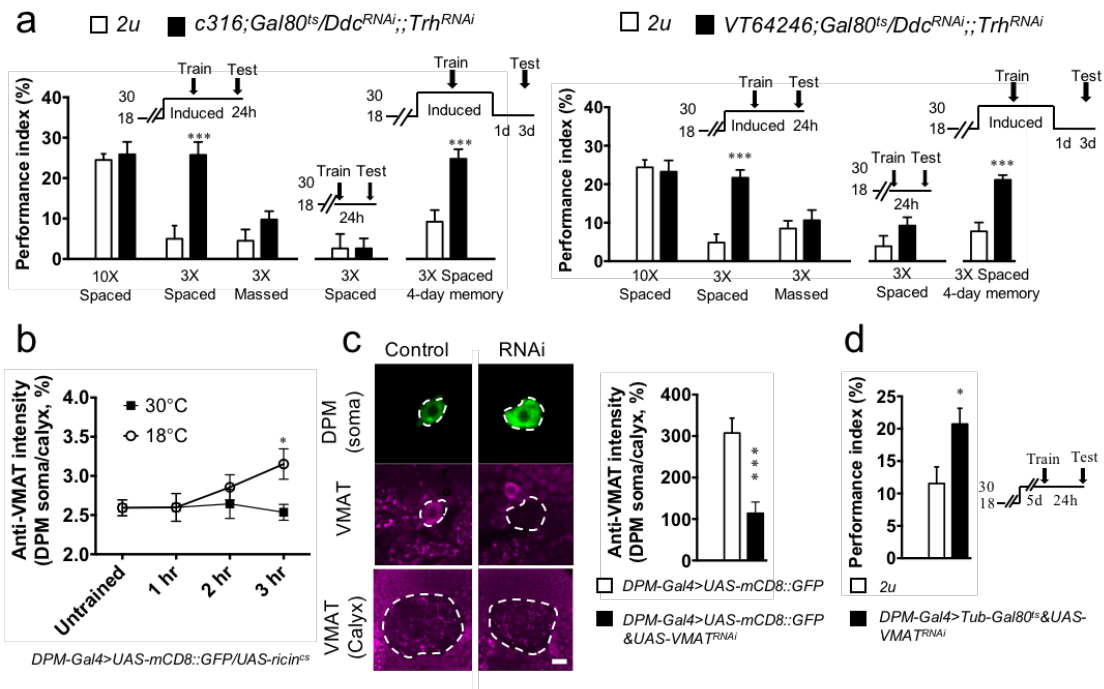
Fig. 3. Serotonin released from dorsal paired medial (DPM) neurons suppresses long-term memory (LTM) formation. (a) Effects of adult-stage specific down-regulation of serotonin synthesis enzymes (Ddc^{RNAi} and Trh^{RNAi}) with two independent *DPM-Gal4* drivers (*c316* and *VT64246*) on 1-day and 4-day memory retention after various training protocols. (b) Changes in VMAT signals in the DPM soma within 3 hours after training. Protein synthesis was blocked by the active ribosomal toxin RICIN^{cs} at 30℃ but unaffected by the inactive RICIN^{cs} at 18℃. (c) Effectiveness and specificity. Left, $VMAT^{RNAi}$ (vesicular monoamine transporter) effectively downregulates anti-VMAT immuno-positive signals (magenta) in the DPM cell body (green) but not in the mushroom body (MB) calyx, which is not innervated by the DPM neuron. Right, Quantitative measurements. (d) Adult-stage specific RNAi-mediated downregulation of VMAT in the DPM neuron enhanced 1-day memory (*DPM-Gal4*: *VT64246-Gal4*) (see **Methods** for training protocols). Each value represents the mean ± S.E.M. (n = 8 in **A, B, D,** n = 10 in **C**). *, P < 0.05; ***, P < 0.001.
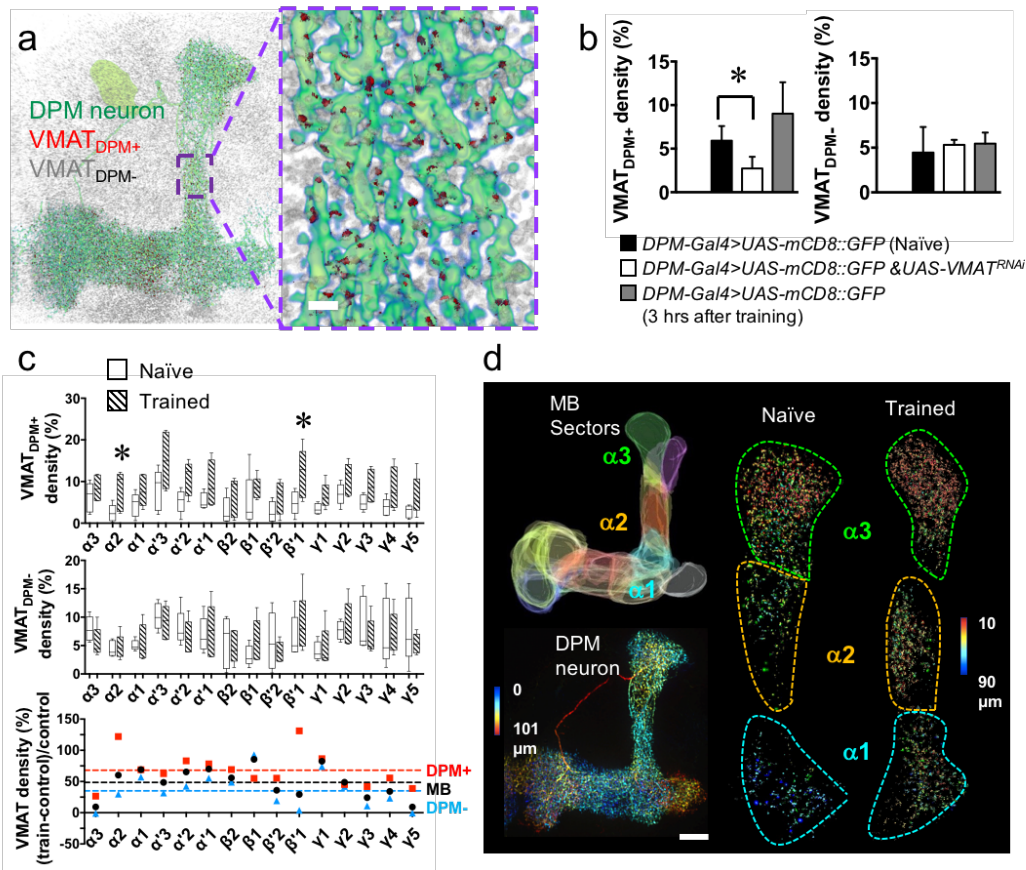
Fig. 4. Training induces sector-specific increases in VMAT expression in axons of DPM neurons. (a) Visualization of VMAT molecules. Left, VMAT proteins (gray) distributed within (red) or outside of (gray) the DPM neurons (green). Right, an enlarged view. **(b)** *VMAT^RNAi*-mediated changes in VMAT density in the DPM+ neurites (left) and DPM- regions (right) within the MB 3 hours after 3x spaced training. **(c)** Comparison of VMAT distribution in DPM axons between naïve and trained flies. VMAT density increases >100% in the $\alpha 2$ and $\beta' 1$ sectors of DPM+ neurites (red) but not DPM- regions (blue) after 3x spaced training. The dashed line indicates the average change among different sectors [Each value represents the mean $\pm$ S.E.M. (n = 6 in **B**; n = 5 in **C**); * = P < 0.05; see **Supplementary Fig**. 8 for calculations]. **(d)** Upper left, a schematic representation of MB sectors. Lower left, a single DPM neuron innervates all MB lobes. Right, a representative volume image shows the

1   training-induced increase in the number of VMAT proteins in the DPM neurites innervating

2   the α2 sector. Color code indicates depth.

3

1   **Methods**

2   **Fly stocks**

3   Fly stocks were raised on cornmeal food at a temperature of 25°C and relative humidity of

4   70% under a 12-h light/dark cycle. The following fly lines were used in the current study:

5   *Fruitless-Gal4* (66696, Bloomington *Drosophila* Stock Center) was used to label neck

6   neurons*, MZ19-Gal4* (34497, Bloomington *Drosophila* Stock Center) was used to label

7   olfactory projection neurons, *12862-Gal4* (111501, DGRC) was used to label giant fiber

8   neurons, *TH-Gal4* (8848, Bloomington *Drosophila* Stock Center) was used to label

9   dopaminergic neurons, *c316-Gal4* (30830, Bloomington *Drosophila* Stock Center) and

10   *VT64246-Gal4* (v204311, VDRC) were used to label DPM neurons, *UAS-mCD8::GFP* (5137

11   and 5310, Bloomington *Drosophila* Stock Center)and *UAS-GCaMP6f* (42747, Bloomington

12   *Drosophila* Stock Center) were used as reporters of Gal4 expression, *UAS-Dscam[1.7]::GFP*

13   (From T. Lee, Howard Hughes Medical Institute, Ashburn, VA) was used to label Dscam in

14   Gal4-labelled neurons, *tub-Gal80^{ts}* (From L. Luo, Stanford University, Stanford, CA) was

15   used to block Gal4 expression at 18°C, *UAS-Ddc^{RNAi}* (3329, VDRC) and *UAS-Trh^{RNAi}* (35240,

16   VDRC) were used to downregulate serotonin expression in DPM neurons, and *UAS-VMAT*

17   *RNAi* (v104072 and v4856, VDRC) was used to downregulate VMAT protein expression in

18   DPM neurons.

19   **Immunohistochemistry**

20   Fly brains were dissected in PBS (pH 7.2) and immediately transferred to a microwave-safe

21   24-well plate containing 4% paraformaldehyde in PBS. The plate was placed on a shaker for

22   25 min. Fixed tissues were then permeabilized and blocked in PBS containing 2% Triton X-

23   100 and 10% normal goat serum (NGS; Vector Laboratories, Burlingame, CA) at 4°C

24   overnight. Immunostaining was sequentially performed in PBS containing 1% Triton X-100

1   and 0.25% NGS using the following primary antibodies: mouse anti-Discs large antibodies

2   (antibody 4F3; 1:20 dilution; Developmental Studies Hybridoma Bank, Iowa City, IA), rabbit

3   anti-GFP antibodies (1:250 dilution; Thermo Fisher Scientific Inc, A11122), rabbit anti-

4   VMAT (1:250 dilution), and secondary antibodies including either biotinylated goat anti-

5   rabbit immunoglobulin G (IgG) (1:250 dilutions; Thermo Fisher Scientific Inc). Biotin-

6   conjugated IgG was detected using Alexa Fluor streptavidin 635 (1:500 dilution; Thermo

7   Fisher Scientific Inc) or HMSiR streptavidin (1:1000 dilution). Each step was carried out

8   over the course of 2 days, with extensive washes between steps at room temperature (25°C).

9   Samples were then transferred to ScaleView-A2 for 2 days before imaging.

10   **HMSiR conjugates**

11   For goat anti-rabbit labelling of HMSiR, we incubated 250 μg of goat anti-rabbit F(ab')2

12   fragment (Jackson Immunoresearch, West Grove, PA) in 0.1 M sodium borate buffer at pH

13   8.5 with 0.8 μl of 10 mM HMSiR-NHS (GORYO Chemical, Bunkyo-ku, Tokyo) in DMSO

14   at 37°C for 30 min, after which the sample was incubated at 4°C overnight. The conjugated

15   antibody was then passed through a Desalt Z-25 column (emp Biotech GmbH, Berlin) to

16   remove unconjugated HMSiR-NHS, and the medium was replaced with PBS (pH 7.2). To

17   label HMSiR with streptavidin, we incubated 125 μg of streptavidin (Sigma-Aldrich, St.

18   Louis, MO) in 250 μl PBS at pH 7.2 with 0.8 μl of 10 mM HMSiR-NHS in DMSO, after

19   which we utilized the same protocol as that used for antibody labelling. Concentrations were

20   then measured at an absorbance of 280 nm, after which the HMSiR conjugates were stored at

21   4°C until use.

22   **Microscope optics and image acquisition**

23   The lasers were combined with long-pass dichroic filters and aligned collinearly before

24   entering an acousto-optical tunable filter (AOTF), which is used to control laser exposure

1   time and wavelength. The laser beam passing through the AOTF was expanded to 4 mm full

2   width at half maximum (FWHM) to distribute the energy evenly onto the annular ring pattern

3   at the quartz mask for creating the illumination pattern conjugated to the back focal plane of

4   the objective lens. To conjugate the illumination pattern to the scanning mirrors, a pair of

5   lenses aligned in 4F geometry was inserted between the mask and scanning mirrors (L12,

6   L13, **Fig. 1a**). Another 4F lens pair was inserted between the galvo mirrors to relay the

7   pattern (L14, L15**, Fig. 1a**). After reaching the scanning mirror (Cambridge Technology,

8   6215H), the pattern was magnified and conjugated to the back aperture of the excitation

9   objective through another pair of lenses (L16, L17, **Fig. 1a**). A dip-in objective was placed

10   perpendicular to the illumination plane to collect the fluorescence signal. Using a piezo

11   scanner (Physik Instrumente, P-725.4 PIFOC), the detection objective was moved in

12   synchrony with the position of the lightsheet, which was controlled by the scanning mirror.

13   Between the individual volumetric scans, an additional settle time on the order of

14   milliseconds was included to stabilize the piezo scanner.

15   The length of the self-reconstructing axial extent of the Gaussian-Bessel lightsheet can

16   be controlled by the geometry of the illumination pattern[16]. A ring-shaped illumination will

17   transform into a concentric irradiance profile distributed along the radial direction around the

18   optical axis at the focal plane of the excitation objective lens. The illumination profile and the

19   total power carried by the Bessel beam are controlled by the diameter and thickness of the

20   annular ring. In the present study, the geometry of the illumination pattern was chosen based

21   on a balance between the area of coverage and the power density of the lightsheet. To achieve

22   stochastic blinking with reasonable signal to noise ratio (SNR), it is necessary to fill the

23   observation plane with a power density above $40W/cm^2$. To localize subareas within the fruit

24   fly brain, we used a lightsheet with an axial FWHM of 50 μm (outer N.A. = 0.26, inner N.A.

25   = 0.185).

1   As the size of the observation area increases, however, the power density of the lightsheet

2   created by simply filtering the laser profile using an annular ring mask is insufficient for

3   providing high precision localization because of the decreasing SNR, as the annular ring

4   intrinsically filters out the most intense component from the Gaussian irradiance profile (**Fig.**

5   **1d2, e1**). In this optical configuration, the field-of-view (FOV) cannot be extended further.

6   We therefore used an axicon lens (Thorlabs) to concentrate the laser energy into a ring

7   pattern, following which the unwanted components were filtered using an annular ring mask

8   (outer N.A. = 0.187, inner N.A. =0.174). The length of the lightsheet generated by the axicon

9   lens can extend to over 200 μm to cover the entire cross section of the fruit fly brain while

10 maintaining a sufficient power density to excite HMSiR (**Supplementary Fig. S1d3, e2**).

11   Choice of the objective lens pair depends on the type of immersion medium. In PBS, a

12 customized excitation objective (Special Optics, 0.65 NA, 3.74 mm WD) was used for image

13 acquisition, while a water immersion detection objective lens (Nikon, CFI Apo LWD 25XW,

14 1.1 NA, 2 mm WD) was used for signal collection. For image acquisition in ScaleView-A2,

15 the excitation objective lens was replaced by a customized objective lens (N.A. = 0.5,

16 working distance = 12.8 mm; NARLabs, ITRC, Taiwan, **Fig. 1b**) designed to optimize

17 performance in media with a higher refractive index (n = 1.38). An immersion detection

18 objective (Olympus, XLPLN25XSVMP2, 25X, 1.0 NA) was used for single-molecule

19 detection in the high-refractive index medium. In the present study, the lightsheet system

20 was carefully calibrated to facilitate single-molecule detection with respect to each of the

21 experimental conditions. As shown in Extended Data Fig. 1, the point spread function (PSF)

22 values from different system configurations were compared to quantify the image quality of

23 the lightsheet microscope system.

24   Single molecule fluorescence was detected using a sCMOS camera (Hamamatsu, Orca

25 Flash 4.0 v2 sCOMS) equipped with a tube lens (f = 500 mm). The exposure time of each

1   frame is typically 100 ms, while the period of an individual volume stack is approximately 40

2   s (400 layers in one stack).

3   Samples were loaded onto 5-mm round glass coverslips (Warner Instruments) using 100

4   nl of Cell-Tak^{TM} (Corning®). During image acquisition, samples and both objectives were

5   immersed in a chamber to maintain optical clarity. All experiments were conducted at room

6   temperature.

7   The use of a Bessel beam lightsheet allows for single-molecule localization even when

8   tissues are maintained in PBS, although the uncertainty of molecule localization increases

9   along with the depth of the illumination plane (**Supplementary Fig. 3a, Supplementary**

10   **Movie 1**). This increases the full-width at half-maximum intensity and reduces image quality

11   in the brain, compared to images acquired from the relatively thinner neck (**Supplementary**

12   **Fig. 3b**). To achieve single-molecule localization in deep tissues, we integrated the lightsheet

13   with optical tissue clearing technology[45,46]. When the fly brain is cleared with neutral

14   ScaleView-A2 solution[18], the Bessel lightsheet provides enough energy to excite a dense

15   population of HMSiR fluorophores at high efficiency throughout the entire brain. As

16   expected, blinking signals are much clearer in ScaleView-A2 than in PBS, especially beyond

17   a depth of 30 μm (**Supplementary Fig. 4**). Moreover, the localization uncertainties remain

18   invariant as the imaging depth increases (**Fig. 1d**). This single-molecule DLM imaging

19   method allows for the three-dimensional reconstruction of olfactory projection neurons,

20   whose axons extend from the antennal lobe at the frontal surface of the brain to the calyx at

21   the posterior surface (**Supplementary Fig. 5a).** With over 50 million molecules localised at a

22   lateral precision of approximately 30 nm, the quality of these DLM images represents a

23   substantial improvement over conventional lightsheet images acquired using the same optical

24   parameters (**Supplementary Movie 2**).

25   **Image processing and rendering**

1   Localization images were reconstructed using ThunderSTORM[19], an ImageJ plugin with a

2   self-built macro for batch processing of massive data. As schematically depicted in

3   **Supplementary Fig. 2**, data were initially transposed to time lapse series on a local

4   workstation, after which they were transferred to remote Lustre storage and distributed to a

5   three-node Torque cluster (Intel Xeon X5660 with 48 GB memory each, connected to Lustre

6   storage). After a particle list was generated for each layer, the list was deposited into one of

7   the clusters, after which a single list containing all localization events within the imaging

8   volume was generated. The list was then used to render the reconstruction image for

9   presentation and analysis. ThunderSTORM was used to perform drift correction using

10   fiducial marker tracking or the cross-correlation method. For three-dimensional volume

11   rendering, the image stack was resampled to minimize discontinuities in structural integrity.

12   We used the Material Statistics module in Avizo 9.4 (Thermo Fisher Scientific Inc) to

13   quantify the volume of MB sectors, DPM neurons and VMAT protein expression. This

14   module calculates the voxel numbers inside a labeled area, which can be transformed into

15   volumes by multiplying by a known voxel size in each image. We manually segmented the

16   boundaries of MB sectors using the Lasso tool in segmentation mode. We used the Magic

17   Wand tool to select one seed within the DPM neuron and to determine a reasonable threshold

18   for selecting connecting voxels. We directly used the threshold tool for whole-volume

19   VMAT images, setting the lower bound to 78 (8-bit; 0-255).

20   **Analysis of image acquisition speed and resolution**

21   Resolution in localization microscopy is governed by localization precision and the density of

22   localization events. When resolving novel structures, an extremely high localization density

23   is required[13]. Very long image acquisition times are required for this outcome, however,

24   which slows experimental throughput. To determine a realistic acquisition time with a

25   reliable statistical basis, we plotted resolution with respect to time. For localization of VMAT

1 expression in DPM neurons, localization density (number of localization events/area of the

2 structure) increases exponentially with acquisition time. As the number of sampling frames

3 increases, the growth of localization density slows due to photo-bleaching and depletion of

4 dye molecules (**Supplementary Fig. 9a**). The theoretical resolution limit is estimated by the

5 localization precision and the Nyquist resolution[47,48]. Resolution power increases rapidly in

6 the first 300 frames (**Supplementary Fig. 9b**). Afterwards, resolution power slows and

7 finally converges at 86 nm. This represents a lower bound of structural resolution that can be

8 achieved with our current methods.

9 More generally, if an infinite photon budget existed and no photo-bleaching occurred,

10 localization density would increase monotonically with the number of sampling frames. Such

11 modeling indicates that resolution reaches 25 nm when 10,000 frames per layer are used in

12 reconstruction—which is 20 times the acquisition time used in this study. Our observed

13 dependence of resolution on sampling frames reveals an exponential relation (likely due to

14 photo-bleaching and limited photon budget; **Supplementary Fig. S9c**), which suggests that

15 the acquisition time required for maximal resolution may be much longer.

16 Fourier ring correlation (FRC) provides a quantitative determination of the structural

17 characteristic in the reconstructed image[49]. The FRC value at the 1/7 cutoff frequency in

18 VMAT protein localization is 283.6 ± 69.9 nm (**Supplementary Fig. 9d**). It should be noted

19 that FRC analysis is based on weighting of the spatial frequency domain and is dominated by

20 the primary feature within the image. As shown in the inset of (**Supplementary Fig. 9d**),

21 VMAT protein presents an island feature with a dimension from hundreds of nanometers to

22 micrometer, which leads to a higher estimated FRC value.

23 When considering the statistics of localizing VMAT molecules, the distribution of VMAT is

24 confined to DPM axons. Consequently, the reliability of the results is dominated by

25 localization precision rather than structural determinations. Regardless, we kept the number

1   of frames of time-lapse data used in VMAT localization to 400 to 500 per layer to ensure all

2   analyses were performed based on similar localization density and theoretical resolution.

3   Acquisition time for one VMAT dataset was approximately 5.6 hours (100 ms per frame, 401

4   frames per imaging volume, 500 volumes recorded). For localization of anti-TH signals (**Fig.**

5   **2**), acquisition time was approximately 5.8 hours (80 ms per frame, 521 frames per imaging

6   volume, 500 volumes recorded). With four sub-volumes per whole brain, total acquisition

7   time took approximately 23.2 hours to complete.

8   ***Drosophila* memory assay**

9   Flies were subjected to aversive olfactory conditioning 2 to 5 days after eclosion. Prior to

10   conditioning, flies were accommodated to a behavioral room with a temperature of 20℃ and

11   relative humidity of 70% for 30 min. At the start of olfactory conditioning, approximately 80

12   flies were transferred to the training tube, after which two aversive odors (3-octanol (OCT);

13   dilution: 1.5 x 10^{-3}; Sigma-Aldrich) and 4-methylcyclohexanol (MCH); dilution: 1.0 x 10^{-3};

14   Fluka) were delivered successively in a current of air (750 ml/min) for 60 s at intervals of 45

15   s. The first odor (CS+) was paired with 12 pulses of electric foot shock at 65 V (serving as

16   the unconditioned stimulus [US]), while the second odor (CS-) was not. This process

17   represented a single session of training. In our experiment, we conducted three sessions of

18   spaced training, with a 10-min interval between each cycle.

19   *Gal4* expression was inhibited by *Gal80^{ts}* by maintaining flies at 18°C. One day before

20   training, flies were moved from 18℃ to 30℃, thereby deactivating *Gal80^{ts}*. Control flies

21   were maintained at a constant temperature of 18℃. Wild-type and experimental flies carrying

22   the same transgenes were trained using several different protocols: three spaced sessions (3x

23   spaced), three massed sessions (3x massed), or 10 spaced sessions (10x spaced).

24   **Statistical analysis**

1 For behavioral experiments, control and treatment groups were tested together (balanced and

2 blinded), with sample sizes listed in figure legends. Because performance indices were

3 normally distributed, the significance of each treatment-versus-control paired comparison

4 was tested using a two-tailed Student's t-test, with P values indicated in figures.

5

6 **Reference:**

7 45 Richardson, D. S. & Lichtman, J. W. Clarifying tissue clearing. *Cell* **162**, 246-257 (2015).

8 46 Chiang, A. S. *et al.* Three-dimensional mapping of brain neuropils in the cockroach,

9   *Diploptera punctata*. *J Comp Neurol* **440**, 1-11 (2001).

10 47 Shroff, H., Galbraith, C. G., Galbraith, J. A. & Betzig, E. Live-cell photoactivated

11   localization microscopy of nanoscale adhesion dynamics. *Nat Methods* **5**, 417-423 (2008)

12 48 Shim, S. H. et al. Super-resolution fluorescence imaging of organelles in live cells with

13   photoswitchable membrane probes. *Proc Natl Acad Sci U S A* **109**, 13978-13983 (2012).

14 49 Nieuwenhuizen, R. P. et al. Measuring image resolution in optical nanoscopy. *Nat*

15   *Methods* **10**, 557-562 (2013).